ELSEVIER

Contents lists available at ScienceDirect

Extreme Mechanics Letters

journal homepage: www.elsevier.com/locate/eml



Data-driven and topological design of structural metamaterials for fracture resistance



Daicong Da, Yu-Chin Chan, Liwei Wang, Wei Chen*

Department of Mechanical Engineering, Northwestern University, Evanston, IL 60208, USA

ARTICLE INFO

Article history:
Received 2 July 2021
Received in revised form 18 October 2021
Accepted 22 October 2021
Available online 16 November 2021

Keywords: Data-driven methods Topological design Structural metamaterials Brittle fracture Stress

ABSTRACT

Data science as a promising paradigm provides novel and diverse opportunities for structural metamaterials attaining exceptional mechanical properties. It is demonstrated here that porous structures composed of brittle constitutive materials can be strong and tough through topological optimization and data-driven techniques. We show that brittle fracture properties can be tailored through the linear control of the homogenized stress and non-periodic microstructures from a multiscale perspective. These tough advanced structural metamaterials pave the way to multiscale components with exceptional fracture resistance.

© 2021 Published by Elsevier Ltd.

1. Introduction

It is well-known that stress concentration will cause premature fracture of any bearing structural materials. Avoiding such a phenomenon is among the most important criteria to design a structure in engineering. However, controlling the stress distribution from a multi-scale perspective has not yet been explored. Besides, establishing inverse design optimization frameworks to support the creation of structural metamaterials with optimal architectures and fracture resistance is still in its infancy.

Topological optimization is an inverse design method that tailors the morphology of the structure by distributing materials inside a given domain under constraints like equilibrium and boundary conditions. Initially flourishing in stiffness optimization, it has been extended to tailor material microstructures to achieve prescribed or extreme constitutive properties [1,2]. Recently, structural fracture resistance design has attracted some attention. In this direction, early works combine explicit crack initiation and propagation with structural design for fracture resistance [3,4]. Later on, gradient-based topology optimization frameworks are proposed, where fracture simulation accounts for the entire failure process involving multiple crack types, while distributions of the constituent materials are tailored to enhance mechanical fracture properties [5–9]. For instance, designing the architecture of the soft constituent in biomimic composites [10] enables energy dissipation ahead of the crack tip to prevent crack propagation and toughen the composite.

* Corresponding author.

E-mail address: weichen@northwestern.edu (W. Chen).

On the other hand, fracture-related design of structural materials has also been addressed by introducing stress constraints to prevent material failure [11,12]. Thereafter, the stress-based topological optimization for specific objectives (e.g. minimal mass, maximal stiffness or minimal overall stress) have been extensively investigated (see, e.g., [13]). This approach is similar to fracture resistance design from the perspective of alleviating the stress concentration around the crack tip such that the crack initiation is prevented, enhancing the fracture performance. Ref. [14] validated that the stress-based optimal structures achieve improved strength and toughness compared with other designs such as the stiffness-oriented solutions. However, both stress and failure process-based fracture resistance optimization have thus far been locked in a single-scale framework. Topological design of the material microstructures to enhance the fracture mechanical properties is, to our best knowledge, investigated here for the first time. Moreover, the ability of optimized nonperiodic porous structures to achieve even further improvement in fracture properties is demonstrated.

Fracture resistance design from a multiscale perspective is a challenging topic, mainly due to the lack of robust multiscale methods for fracture simulation in the presence of complex heterogeneous media. In addition, numerical optimization is difficult with such a high-dimensional problem where heterogeneous materials and structures acting at different scales need to be optimized simultaneously. Under this stalemate, data-driven methods came into being, providing novel and prosperous ways for multi-scale design optimization, e.g. in reducing dimensionality [15] and accelerating the design of nanocomposites [16] and multiscale structures [17]. For the first time, this work combines

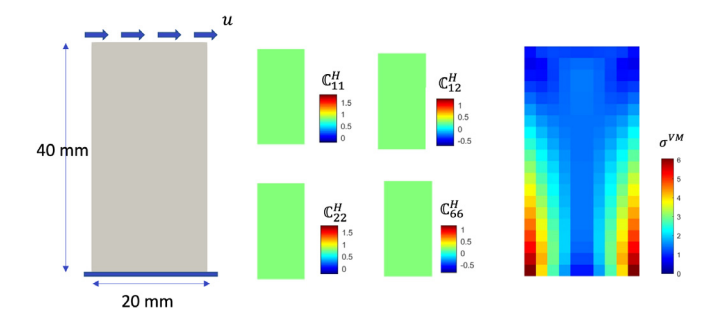


Fig. 1. Illustration of the design domain and shear loading boundary conditions (left); initial stiffness tensor distribution (middle); and the corresponding homogenized global stress distribution (right).

data-driven and topology design methods to optimize the microstructure of materials by maximizing the uniform distribution of the macrostructural stress, thus toughening and strengthening the global (macroscopic) porous structure composed of brittle constituent materials.

Three steps are implemented to validate the enhancement of the fracture toughness of the porous structures. Firstly, a multiscale inverse optimization framework is established to precisely control the global stress by tailoring the distribution of the components of the homogenized stiffness tensor. Thereafter, the architecture of each unit cell is identified from a large database via data-driven techniques while guaranteeing the connectivity between neighboring cells. Finally, the fracture resistance performance of the assembled structure is validated through the phase field method [18–21].

2. Stress control

For a given global macroscopic structure under specific boundary conditions, e.g., Fig. 1, its stress distribution and fracture resistance are highly dependent on its microscopic geometries. The first goal is to establish an inverse topology optimization framework to control the stress distribution by tailoring the geometries of material microstructures. The final morphology of microstructures will be pulled from a database which contain both the information of the geometries and the corresponding homogenized effective properties, i.e., the apparent elastic moduli $\mathbb{C}^{\textit{Hom}}$. Therefore, each component of the elastic moduli $\mathbb{C}^{\textit{Hom}}$ is used as a design variable, and they will be updated independently during the optimization process. Note that only orthotropic microstructural geometries are considered in this work, so only four components (design variables), \mathbb{C}^{Hom}_{11} , \mathbb{C}^{Hom}_{12} , \mathbb{C}^{Hom}_{22} , and \mathbb{C}^{Hom}_{66} will be tailored. However, fully anisotropic geometries and composite unit cells can be considered in future work with promising perspectives.

In Fig. 1, the load and boundary conditions of the global structure are schematized, where the bottom edge is fixed, and a rightward incremental displacement load is applied to the top boundary. The aspect ratio of the global structure is 1:2, and the structure is discretized into 10×20 quadrilateral four-node elements. Homogeneous initial values of the design variables are shown on the middle of Fig. 1. The corresponding initial stress state at the macroscopic scale is shown on the right, where the maximum stress value is equal to 6.0717. Note that the stress distribution computed here is the von Mises stress of each finite element and measured by

$$\sigma^{\text{VM}} = \sqrt{\frac{3}{2}\sigma':\sigma'}, \text{ with } \sigma'_{ij} = \sigma_{ij} - \frac{1}{3}\delta_{ij}\sigma_{kk}$$
 (1)

The Kronecker delta δ_{ij} serves as the identity matrix **1** based on its properties that it equals to 1 when i=j and 0 otherwise. In 2D scenarios, with $\sigma_{zz} = \tau_{xz} = \tau_{yz} = 0$, the von Mises stress reads

$$\sigma_{\text{VM}} = \sqrt{\sigma_{xx}^2 + \sigma_{yy}^2 - \sigma_{xx}\sigma_{yy} + 3\tau_{xy}^2} \tag{2}$$

or

$$\sigma_{\text{VM}} = (\boldsymbol{\sigma}^T \mathbf{M} \boldsymbol{\sigma})^{1/2}, \quad \mathbf{M} = \begin{bmatrix} 1 & -1/2 & 0 \\ -1/2 & 1 & 0 \\ 0 & 0 & 3 \end{bmatrix}$$
 (3)

Firstly, we design the macroscopic stiffness component such that the maximum stress of the global structure will reach a given specific value. Therefore, the objective function can be formulated as

$$\min_{\mathbb{C}_{11}^{Hom}, \mathbb{C}_{12}^{Hom}, \mathbb{C}_{22}^{Hom}, \mathbb{C}_{66}^{Hom}} f = (\sigma_{\text{VM}, \text{max}} - \sigma^*)^2$$

$$\tag{4}$$

where $\sigma_{\rm VM,max}$ is the maximum value and σ^* is the given threshold. However, both values are discrete data and not differentiable, which means that gradient-based optimization methods cannot be adopted to solve the problem. To overcome this issue, the maximum value is aggregated by the so-called *P*-norm stress aggregation function [12] formulated as

$$\sigma_{\text{VM,max}} \approx \sigma_{\text{PN}} = (\sum_{e}^{N_e} \sigma_{\text{VM},e}^P)^{1/P}, \quad e = 1, \dots, N_e$$
 (5)

where σ_{PN} is the P-norm global stress measure, P is the constant parameter, and N_e is the total number of finite element discretizing the domain. It is known that a larger P value is preferable to approximate the maximum stress more accurately, but it may also lead to numerical problems in updating the pseudo density in general stress-based topology optimization [12]. However, the latter is naturally avoided in our optimization where the design variables are defined as the true components of the effective material properties which can be tailored among possible solutions from our database without resulting in the ill-conditioned problems. Based on our numerical experiments, a relatively large number, P = 66, is adopted throughout the provided examples to ensure that the error between σ_{PN} and $\sigma_{VM,max}$ is small (e.g., within 1%). Hereafter, the objective function in (4) will be equivalently expressed as $f = (\sigma_{PN} - \sigma^*)^2$, and sensitivity of the objective function w.r.t. the design variable is detailed in Appendix A.

To validate our optimization framework, four different cases are considered, in which the specific target value σ^* is set as 5.0, 6.5, 8.5, and 10.0, respectively. The macroscopic stress distribution is shown on the left side in each case in Fig. 2, while the optimized stiffness tensor is shown on the right. As observed, the maximum stress values are 4.9963, 6.5008, 7.9997, and 10.0056, respectively, which are very close to the corresponding thresholds. This is attributed to the subversively different distribution of the stiffness tensor. We therefore first demonstrate that we can effectively control the homogenized stress state inside the macroscopic structure by tailoring the elemental stiffness tensor aroused from the microscopic materials.

3. Database

Next, we will find the target microscopic unit cell in each finite element based on the data-driven method. The targeted unit cells are selected from the database to achieve the optimal distribution of the stiffness tensor and then assembled into the macroscopic global structure. The database of more than 160,000 unit cells, which can be found at https://github.com/Daicong-

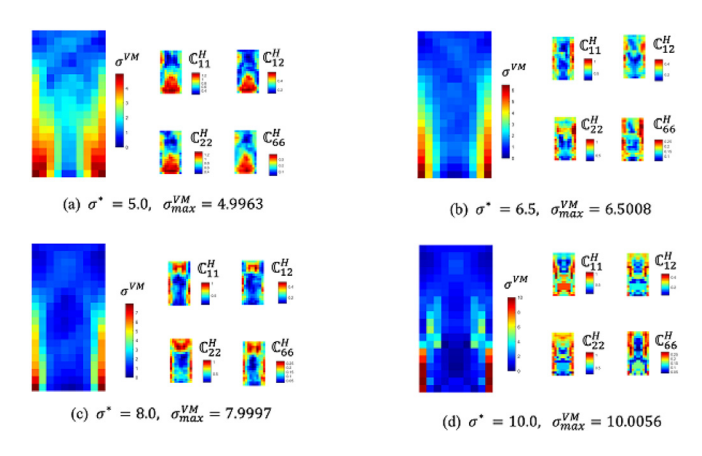


Fig. 2. Optimized components of the stiffness tensor and the corresponding macroscopic stress distribution.

Da/2D-Orthotropic-Unit-Cell-Dataset.git, is illustrated in Fig. 3. displaying that the constructed database covers a large portion of the possible optimal properties. The detailed procedure to generate the meaningful unit cells can be found in our previous work [22,23]. In Fig. 3(d), the volume fractions of all unit cells range between 0.2 and 1. For each unit cell, the corresponding effective stiffness tensor \mathbb{C}^{Hom} was computed by the numerical homogenization method [24] and stored in the database so that they can be quickly retrieved during design. The computation is performed for elementary load cases in a standard homogenization scheme consisting of unit tensile strain and pure shear loading. Since multiple geometries of the unit cell can possess the same values of the apparent elastic moduli \mathbb{C}^{Hom} , the unit cells with the best connectivity between their neighborhood and that satisfy the optimized properties are selected through a graph labeling. Specifically, we construct a grid-like weighted graph where each node represents a unit cell, and edges connect adjacent cells. Then the unit cell assembly problem can be regarded as selecting an index from the given database to label each node in the graph. Within this setting, the distance between the target property and the one of the unit cell to be selected is designated as the node weight, and the discrepancy between adjacent nodes is designated as the weight of each edges. Thereafter, the dual decomposition Markov random field (DD-MRF) method [25] can be used to effectively find the best labels of the graph with the smallest sum of node and edge attributes, to identify the macrostructure that satisfies the target properties and ensures connectivity.

4. Fracture resistance validation

For the fracture resistance validation, the number of the microscopic unit cells in the macrostructure of Fig. 1 is first selected as 5 by 10, in the x- and y- directions, respectively. As baselines, two classical shapes, structures A and B, are chosen, and they are depicted in Fig. 4(a) and (b), respectively. The non-periodic structure (c) is designed via the proposed data-driven and topological optimization framework to minimize the maximum stress in Eq. (5), where the objective function is formulated as:

$$\min_{\substack{\mathcal{C}_{11}^{Hom}, \mathcal{C}_{12}^{Hom}, \mathcal{C}_{66}^{Hom}, \mathcal{C}_{66}^{Hom}}} f = \sigma_{\text{VM}, \text{max}}$$
 (6)

The volume fractions for all the structures are fixed as 0.5. Excellent consistency between the different unit cells can be well observed in Fig. 4(c).

We use the phase field method (see details in Appendix B) to validate the improvement of the fracture resistance of the

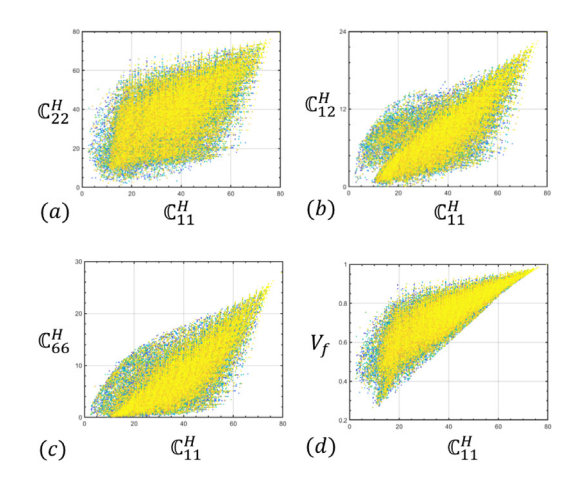


Fig. 3. The constructed database: (a)–(c) different stiffness tensor components versus each other; (d) the volume fraction V_f versus the component \mathbb{C}_1^{Hom} .

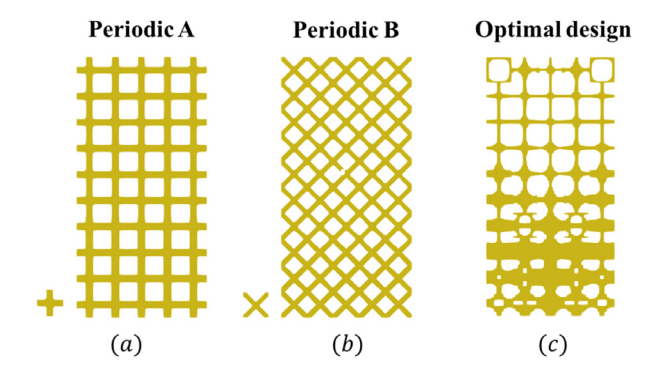


Fig. 4. (a) classical periodic Structure A; (b) periodic Structure B; (c) optimized non-periodic structure by the proposed framework.

optimized structure compared to classical periodic structures. The isotropic brittle solid material inside the global structure has Young's modulus E=72, Poisson's ratio $\nu=0.29$, and critical energy release rate $G_c = 0.442e - 3$. Final crack patterns of the three macrostructures are shown in Fig. 5(a), (b), and (c), corresponding to the displacement at 0.225, 0.335, and 0.49, respectively. It first indicates that the optimized structure possesses the largest failure displacement. In addition, the damage locations of the two periodic structures are initiated near the bottom edges, while it is in the upper half of the optimal design. Detailed force-displacement curves are compared in Fig. 5(d), and amplifications of the mechanical properties including the stiffness (E), toughness (T), strength (S), and failure displacement (D) of all the structures compared with Structure A are displayed in Fig. 5 (e). Here, the stiffness (E), i.e., "reciprocal" of the widely accepted compliance in most topology optimization literature, is computed by the slope of the rising curve. The toughness (T) is measured by the total area of each load-displacement curve. The strength (S) is simply defined as the peak load of each curve, and the failure displacement (D) is the largest deformation that the structure can withstand before its rupture.

Firstly, the periodic Structure A does have the largest stiffness and highest strength. However, this structure is the first to break because of the conflicting nature between strength and toughness [26]. Compared with the Structure A, the toughness and failure displacement of the periodic Structure B is improved by 8.12% and 47.82%, while the stiffness and strength are decreased by 48.75% and 32.40%, respectively. For the optimized structure based on the data-driven method, the reduction in stiffness is

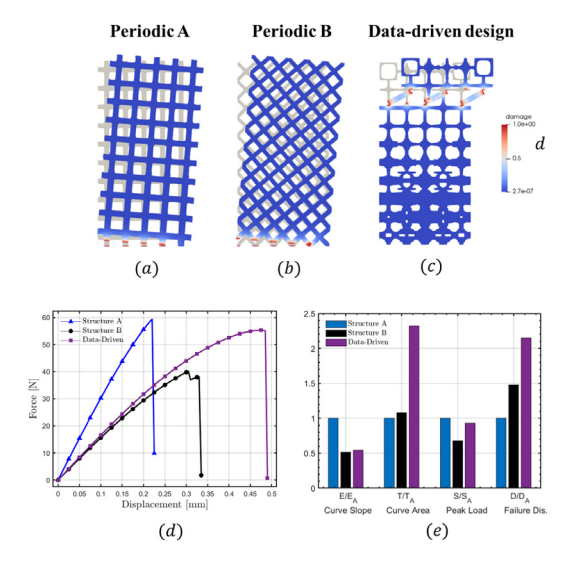


Fig. 5. (a–c): final crack patterns of the three global structures; (d): comparison of the load–displacement curves; (e) amplifications of the mechanical properties compared with the classical periodic Structure A.

similar to that of Structure B, while the strength is decreased by only 6.78% compared to A. On the other hand, the failure displacement of the data-driven design is increased by 115.22%, and the toughness, which is measured based on the total area of the curve, is improved by 131.71%. These improvements are significant and, to a certain degree, overcomes the conflicts between the strength and toughness by postponing the failure of the structure. In other words, the porous structures composed of the brittle constitutive material can be both strong and tough by using our proposed data-driven design technique.

Next, we investigate the size effect of the microscopic unit cells. Instead of the previous 5×10 , a larger number of the unit cells 10×20 is considered. The dimension of the global structure is the same as before, and the length size of the unit cell is therefore reduced by half. We repeat all the previous cases and show the designed macrostructure with 10×20 unit cells along with its fracture resistance against other structures in Fig. 6. Displayed in the top row of Fig. 6(a) are the geometries of periodic structures A and B as well as the data-driven aperiodic design. To quantify the introduced error of substituting the optimized material properties by the closest unit cells, we employ the Mean Squared Error (MSE) as the measuring metric, employ the Mean squared Error (MSE) as the measuring metric, i.e., MSE = $\frac{1}{N_e} \sum_{e}^{N_e} (\mathbb{C}_e^H - \widehat{\mathbb{C}}_e^H)^2$, where N_e is the number of unit cells/elements, \mathbb{C}_e^H are the effective properties of the substituted unit cell including \mathbb{C}_{11}^H , \mathbb{C}_{12}^H , \mathbb{C}_{22}^H , and \mathbb{C}_{66}^H , while $\widehat{\mathbb{C}}_e^H$ are the corresponding optimized ones. A small MSE therefore indicates a good substitution of the optimized material properties. The MSE value for the provided structure by the proposed data-driven design in Fig. 6 is 1.84e-4. Excellent match between $\widehat{\mathbb{C}_{11}^H}$ and $\widehat{\mathbb{C}_{11}^H}$ and between $\widehat{\mathbb{C}_{22}^H}$ and $\widehat{\mathbb{C}_{22}^H}$ of the unit cells within the assembled structure is illustrated in Fig. 7.

The final crack patterns of the three porous structures are shown in the bottom row of Fig. 6(a), corresponding to the displacement loading at 0.235, 0.335, 0.46, respectively. Thus, the failure displacement of the data-driven design is elongated by 95.74% and 37.31%, compared with periodic structures A and B, respectively. The strength (S) of the data-driven design is the same as the strongest Structure A, while the toughness is improved by 117.07%. Comparing each case with the same macro dimension but less unit cells (5×10) , the mechanical properties of the periodic structures A and B with different size of the unit

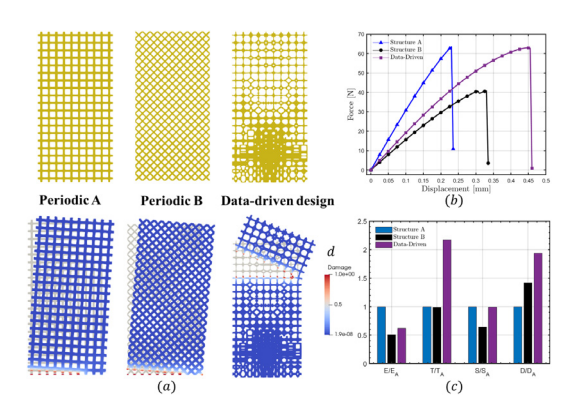


Fig. 6. (a) geometries and final crack patterns of the three macrostructures with 10×20 microscopic unit cells; (b) corresponding force–displacement curves; (c) amplifications of the mechanical properties of all structures compared with the periodic Structure A.

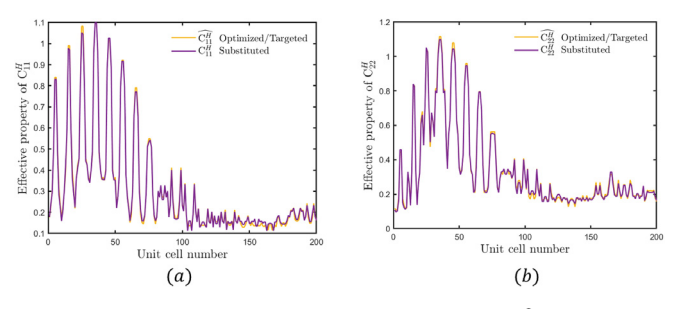


Fig. 7. Illustration of the comparison between (a) optimized $\widehat{\mathbb{C}}_{11}^H$ and substituted $\widehat{\mathbb{C}}_{11}^H$; and (b) optimized $\widehat{\mathbb{C}}_{22}^H$ and substituted $\widehat{\mathbb{C}}_{22}^H$.

cells are almost identical. However, in the data-driven design, the stiffness (E), toughness (T), and strength (S) are improved by 15.86%, 4.07%, and 13.58%, respectively. This is because during the optimization, the homogenized stress is considered at the macroscopic scale, while the structure is assembled by the unit cell in a finite-element-wise way, given the evidence that the scales are not separated. Therefore, with the smaller size of the microscopic unit cell, it is closer to satisfying the scale separation assumption which is essential to the numerical homogenization. On the other hand, with the larger number of unit cells, more design variables are utilized, which contributes to more design freedom and thus ability to obtain a better design.

Finally, we examine the size effect of the global structure itself. Taking the previous data-driven design with 5×10 unit cells (global dimension $20 \times 40 \text{ mm}^2$) as a baseline, we fix the number of unit cells as 5×10 but increase the global size to $40 \times 80 \text{ mm}^2$ and $60 \times 120 \text{ mm}^2$. The final crack patterns of the three global structures with different dimensions are shown in Fig. 8(a). Interestingly, with the larger size, the fracture location is different from that of the smallest global size ($20 \times 40 \text{ mm}^2$), while they are all the same for both structures A and B based on our experiments, illustrating that there is a huge size effect on the data-driven designed structures. Following the fracture size effects analysis in [27], we compute the nominal stress as $\sigma_{nominal} = rac{3FL}{2bH^2}$ for each case with different global sizes, where L and H are the length and height of the global structures, respectively, and b is the thickness and equals to 1 herein. F is the reaction force. The nominal stress-strain curves for the three considered global structures are shown Fig. 8(b). It indicates that the largest global structure is the weakest while the smallest one is the strongest, which is still consistent with the conclusions in [27].

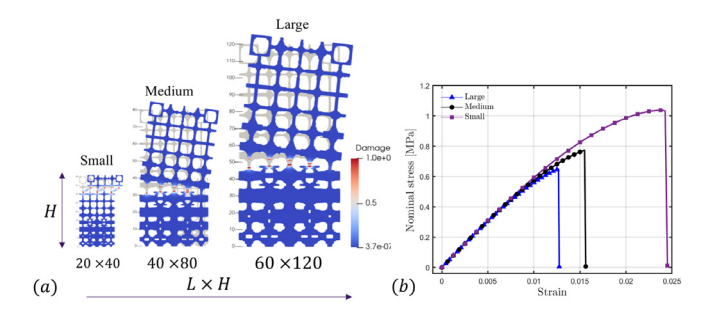


Fig. 8. Size effects of the global structure: (a) final crack patterns of the data-driven designed structures; (b) corresponding nominal stress-strain curves.

5. Conclusions

In summary, we proposed a data-driven design framework for brittle porous structure with the purpose to enhance fracture resistance. The topological-like optimization on distribution of the stiffness tensor components is first established to control the global homogenized stress. Thereafter, data-driven techniques are used to find the target unit cells with the geometries stratifying the optimal distribution of the stiffness tensor. Then, the macroscopic structure is assembled by the target unit cells, where the good connectivity between neighboring cells is guaranteed. Finally, phase field fracture simulation is conducted for the data-driven design and illustrates that the fracture resistance can be significantly enhanced compared with the classical periodic structures.

It is demonstrated that the fracture properties of the brittle structural materials can be optimally tailored through stress control, topology optimization, and data-driven techniques. Conflicts between strength and toughness of brittle materials are overcome by maximizing the uniform distribution of the macrostructure stress, i.e. minimizing the maximum stress to avoiding the stress concentration. By doing this, it postpones the crack initiation during continuous loading and therefore toughens the brittle structural materials.

In addition, both size effects on the global structures and on the microscopic unit cells are investigated. Through optimization, global structures with smaller size unit cells may have better fracture resistance because of the greater design freedom and homogenized size effects. Last but not least, the larger size of the global structure will be weaker for both periodic and data-driven designed aperiodic structures. However, the fracture location is completely changed when the size changes for the optimal design, displaying a huge size effect of the data-driven structures and indicating the extreme designability of fracture resistance at different scales. Future work will consider material and/or geometric nonlinearities, and conduct physical experimental verification on samples fabricated by using additive manufacturing.

Declaration of competing interest

The authors declare that they have no known competing financial interests or personal relationships that could have appeared to influence the work reported in this paper.

Acknowledgments

We gratefully acknowledge the financial support of the NSF CSSI program (Grant No. OAC 1835782). Yu-Chin Chan thanks the NSF Graduate Research Fellowship (Grant No. DGE-1842165).

Appendix A

The derivative of the *P*-norm global stress measure σ_{PN} in (5) w.r.t. the design variable, i.e., *ij*th component of the macroscopic stiffness of element e ($\mathbb{C}_{e,ii}$) reads:

$$\frac{\partial \sigma_{\text{PN}}}{\partial \mathbb{C}_{e,ij}} = \sigma_{\text{PN}}^{1-P} \left(\sum_{e} \sigma_{\text{VM},e}^{P-1} \frac{\partial \sigma_{\text{VM},e}}{\partial \mathbb{C}_{e,ij}} \right) \tag{7}$$

Using the von Mises formulation (3), the derivative of the von Mises stress w.r.t. the stress vector first reads

$$\frac{\partial \sigma_{\text{VM}}}{\partial \boldsymbol{\sigma}} = (\boldsymbol{\sigma}^T \mathbf{M} \boldsymbol{\sigma})^{-1/2} \boldsymbol{\sigma}^T \mathbf{M}$$
 (8)

Therefore, the term $\frac{\partial \sigma_{\text{VM},e}}{\partial \mathbb{C}_{e,ij}}$ in (7), i.e. the derivative of elemental von Mises stress w.r.t. the *ij*th component of the macroscopic stiffness $\mathbb{C}_{e,ij}$ reads

$$\frac{\partial \sigma_{\text{VM},e}}{\partial \mathbb{C}_{e,ij}} = \sigma_{\text{VM},e}^{-1} \sigma_e^T \mathbf{M} \frac{\partial \mathbb{C}_e \mathbf{B}_e \mathbf{U}_e}{\partial \mathbb{C}_{e,ij}}$$
(9)

Note that \mathbf{B}_e is the elemental strain–displacement matrix which is independently of the $\mathbb{C}_{e,ij}$. Then, the above formulation can be rewritten as

$$\frac{\partial \sigma_{VM,e}}{\partial \mathbb{C}_{e,ij}} = \sigma_{VM,e}^{-1} \sigma_e^T \mathbf{M} \frac{\partial \mathbb{C}_e}{\partial \mathbb{C}_{e,ij}} \mathbf{B}_e \mathbf{U}_e +
\sigma_{VM,e}^{-1} \sigma_e^T \mathbf{M} \mathbb{C}_e \mathbf{B}_e \frac{\partial \mathbf{U}_e}{\partial \mathbb{C}_{e,ij}}$$
(10)

The first term on the right hand side (RHS) of Eq. (10) can be computed directly. Using $\mathbf{U}_e = \mathbf{L}_e \mathbf{U}$ and $\frac{\partial \mathbf{U}}{\partial \mathbb{C}_{e,ij}} = -\mathbf{K}^{-1} \frac{\partial \mathbf{K}}{\partial \mathbb{C}_{e,ij}} \mathbf{U}$ (assuming that there is no traction or it is constant), the second term becomes

$$-\sigma_{\mathrm{VM},e}^{-1}\sigma_{e}^{T}\mathbf{M}\mathbb{C}_{e}\mathbf{B}_{e}\mathbf{L}_{e}\mathbf{K}^{-1}\frac{\partial\mathbf{K}}{\partial\mathbb{C}_{e}}\mathbf{U}$$

Note again terms **K** and **U** are the global stiffness and displacement matrices, respectively. Therefore, the derivative of the *P*-norm stress measure w.r.t. the *ij*th component of the macroscopic stiffness $\mathbb{C}_{e,ij}$ reads

$$\frac{\partial \sigma_{\text{PN}}}{\partial \mathbb{C}_{e,ij}} = \sigma_{\text{PN}}^{1-P} \left(\sum_{e} \sigma_{\text{VM},e}^{P-2} \sigma_{e}^{T} \mathbf{M} \frac{\partial \mathbb{C}_{e}}{\partial \mathbb{C}_{e,ij}} \mathbf{B}_{e} \mathbf{U}_{e} \right) - \sigma_{\text{PN}}^{1-P} \left(\sum_{e} \sigma_{\text{VM},e}^{P-2} \sigma_{e}^{T} \mathbf{M} \mathbb{C}_{e} \mathbf{B}_{e} \mathbf{L}_{e} \right) \mathbf{K}^{-1} \frac{\partial \mathbf{K}}{\partial \mathbb{C}_{e,ij}} \mathbf{U}$$
(11)

where $e = 1, ..., N_e$ and i, j = 1, 2, 3. The second term on the RHS of (11) requires to solve the following adjoint equation

$$\mathbf{K}\lambda = \sum_{e} \sigma_{\mathrm{VM},e}^{P-2} (\mathbb{C}_{e} \mathbf{B}_{e} \mathbf{L}_{e})^{T} \mathbf{M} \sigma_{e}$$
 (12)

Finally, the sensitivity of Eq. (11) which originally from Eq. (7) can be formulated as

$$\frac{\partial \sigma_{\text{PN}}}{\partial \mathbb{C}_{e,ij}} = \sigma_{\text{PN}}^{1-P} \left(\sum_{e} \sigma_{\text{VM},e}^{P-2} \sigma_{e}^{T} \mathbf{M} \frac{\partial \mathbb{C}_{e}}{\partial \mathbb{C}_{e,ij}} \mathbf{B}_{e} \mathbf{U}_{e} \right) - \sigma_{\text{PN}}^{1-P} \boldsymbol{\lambda}_{e}^{T} \frac{\partial \mathbf{K}}{\partial \mathbb{C}_{e,ij}} \mathbf{U} \tag{13}$$

where \mathbf{U}_e and $\boldsymbol{\lambda}_e$ are the elemental displacement and adjoint nodal value vectors associated to the *e*th element, respectively.

Correspondingly, the sensitivity of the objective function f in (4) w.r.t. the ijth component of the macroscopic stiffness $\mathbb{C}_{e,ij}$ reads

$$\frac{\partial f}{\partial \mathbb{C}_{e,ij}} = 2(\sigma_{PN} - \sigma^*) \frac{\partial \sigma_{PN}}{\partial \mathbb{C}_{e,ij}}$$
(14)

Appendix B

For a cracked body, the associated regularized form of total energy in phase field method is defined by:

$$E(\mathbf{u}, d) = \int_{\Omega} \Psi(\boldsymbol{\varepsilon}, d) \, dV + g_c \int_{\Omega} \gamma(d, \nabla d) dV - \int_{\Omega^t} \boldsymbol{t} \cdot \boldsymbol{u} \, dS \quad (15)$$

where $\Omega \subset \mathbb{R}^3$ is a defined cracked domain, and $\Psi(\boldsymbol{\varepsilon},d)$ is the elastic energy density function formulated as

$$\Psi(\boldsymbol{\varepsilon}, d) = g(d)\Psi^{+}(\boldsymbol{\varepsilon}^{+}) + \Psi^{-}(\boldsymbol{\varepsilon}^{-}) \tag{16}$$

Above, g(d) is a degradation function such that g(0) = 1, g(1) = 0and g'(1) = 0. Besides, Ψ^+ and Ψ^- denote the tensile and compressive parts of the strain density function, respectively, through a decomposition of the elastic strain. The second part on the right of (15) corresponds to the energy required to create crack according to the Griffith criterion, where g_c is the critical fracture energy density and also named as Griffith's critical energy release rate. $\gamma(d, \nabla d)$ is the crack surface density function. With sharp cracks denoted collectively as Γ , the second term on the right of (15) will be donated as $\int_{\Gamma} g_c d\Gamma$. t represents any external tractions applied to the body's surface. This phase field formulation implies: (a) minimization of the total energy with respect to the displacement field \boldsymbol{u} and (b) minimization of the energy with respect to the scalar field d describing the crack surface in a smooth manner. The second minimization is subjected to an inequality constraint: $\dot{d} \geq 0$, and the time-step $\mathcal{T} = \{t^0, t^1, \dots, t^n, t^{n+1}, \dots, t^{N_{load}}\}$ will be introduced to simply formulate the two problems to find the displacement field \boldsymbol{u}^{n+1} and d^{n+1} (in each time step t^{n+1}). Therefore, the mechanical and crack phase field problems are fully coupled, and these two-phase problems will be solved in a sequential or staggered scheme.

For the mechanical problem, at each time step, the linear momentum balance equation for the solid medium without body force reads

$$\nabla \cdot \boldsymbol{\sigma} = \mathbf{0} \tag{17}$$

with

$$\boldsymbol{\sigma} \cdot \boldsymbol{n} = \boldsymbol{t} \text{ on } \partial \Omega_t \text{ and } \boldsymbol{u} = \bar{\boldsymbol{u}} \text{ on } \partial \Omega_u$$
 (18)

where

$$\sigma = \frac{\partial \Psi(\epsilon, d)}{\partial \epsilon} \tag{19}$$

Regarding to the phase field problem, by choosing $\gamma(d)=\frac{1}{2\ell}d^2+\frac{\ell}{2}\nabla d\cdot\nabla d$, the associated Euler–Lagrange equation for the above second minimization at each time step is given by:

$$(2[\Psi^{+}] + \frac{g_c}{I})d - \lg_c \nabla^2 d = 2[\Psi^{+}]$$
 (20)

with

$$\nabla d \cdot \mathbf{n} = 0 \text{ on } \partial \Omega \text{ and } d = 1 \text{ on } \Gamma$$
 (21)

where l is the length scale for characterizing the phase field crack diffusion. $[\Psi^+]$ is the tensile part of the strain energy density through a decomposition. Here, we use the volumetric-deviatoric split/decomposition of the strain energy density as proposed in [28], which reads:

$$\Psi^{+} := \frac{K}{2} \langle tr(\boldsymbol{\varepsilon}) \rangle_{+}^{2} + \mu(\boldsymbol{\varepsilon}^{dev} : \boldsymbol{\varepsilon}^{dev}) \quad \Psi^{-} := \frac{K}{2} \langle tr(\boldsymbol{\varepsilon}) \rangle_{-}^{2}$$
 (22)

with

$$K = \lambda + \frac{2\mu}{n} \quad \langle x \rangle_{\pm} := \frac{1}{2} (x \pm |x|) \quad \boldsymbol{\varepsilon}^{dev} := \boldsymbol{\varepsilon} - \frac{1}{3} tr(\boldsymbol{\varepsilon}) \mathbf{1}$$
 (23)

where K is the material bulk modulus, n is the problem dimension, λ and μ are the Lamé coefficients, and e^{dev} is the deviatoric

strain tensor. Note that other energy distribution ways, e.g. principal/spectral splitting by the strain tensor are also applicable to the above decomposition. Further, to enforce the irreversibility of the crack phase field d, the tensile part of the strain energy Ψ^+ in (20) is replaced by a so-called local history variable field $\mathcal H$ as proposed in [21]:

$$\mathcal{H}(\mathbf{x},t) := \max_{t \in [0,T]} \left\{ \Psi^{+}(\mathbf{x},t) \right\}. \tag{24}$$

As the staggered solution scheme is employed to solve the above coupled problem of fracture, the overall algorithm is defined as follow.

- 1. Set the initial fields $d(t_0)$, $\mathbf{u}(t_0)$, and $\mathcal{H}(t_0)$ at time t_0 .
- 2. **Loop** over all time increments; at each time t_{n+1} :
 - (a) Given $d(t_n)$, $\mathbf{u}(t_n)$, and $\mathcal{H}(t_n)$,
 - (b) Compute the history function $\mathcal{H}(t_{n+1})$ according to (24).
 - (c) Compute the crack phase field $d(t_{n+1})$ by solving (20).
 - (d) Compute $\mathbf{u}(t_{n+1})$ with the current crack $d(t_{n+1})$ by solving (17).
 - (e) $(.)_n \leftarrow (.)_{n+1}$ and go to (a).

3. **End**.

References

- [1] O. Sigmund, Materials with prescribed constitutive parameters: an inverse homogenization problem, Int. J. Solids Struct. 31 (17) (1994) 2313–2329.
- [2] O. Sigmund, Tailoring materials with prescribed elastic properties, Mech. Mater. 20 (4) (1995) 351–368.
- [3] G.X. Gu, L. Dimas, Z. Qin, M.J. Buehler, Optimization of composite fracture properties: method, validation, and applications, J. Appl. Mech. 83 (7) (2016)
- [4] B. San, H. Waisman, Optimization of carbon black polymer composite microstructure for rupture resistance, J. Appl. Mech. 84 (2) (2017).
- [5] L. Xia, D. Da, J. Yvonnet, Topology optimization for maximizing the fracture resistance of quasi-brittle composites, Comput. Methods Appl. Mech. Engrg. 332 (2018) 234–254.
- [6] D. Da, J. Yvonnet, L. Xia, G. Li, Topology optimization of particle-matrix composites for optimal fracture resistance taking into account interfacial damage, Internat. J. Numer. Methods Engrg. 115 (5) (2018) 604–626.
- [7] D. Da, Topology Optimization Design of Heterogeneous Materials and Structures, John Wiley & Sons, 2019.
- [8] C. Wu, J. Fang, S. Zhou, Z. Zhang, G. Sun, G.P. Steven, Q. Li, Level-set topology optimization for maximizing fracture resistance of brittle materials using phase-field fracture model, Internat. J. Numer. Methods Engrg. 121 (13) (2020) 2929–2945.
- [9] D. Da, J. Yvonnet, Topology optimization for maximizing the fracture resistance of periodic quasi-brittle composites structures, Materials 13 (15) (2020) 3279.
- [10] D. Da, X. Qian, Fracture resistance design through biomimicry and topology optimization, Extrem. Mech. Lett. (2020) 100890.
- [11] P. Duysinx, M.P. Bendsøe, Topology optimization of continuum structures with local stress constraints, Internat. J. Numer. Methods Engrg. 43 (8) (1998) 1453–1478.
- [12] C. Le, J. Norato, T. Bruns, C. Ha, D. Tortorelli, Stress-based topology optimization for continua, Struct. Multidiscip. Optim. 41 (4) (2010) 605–620.
- [13] C. Wang, X. Qian, Heaviside projection-based aggregation in stress-constrained topology optimization, Internat. J. Numer. Methods Engrg. 115 (7) (2018) 849–871.
- [14] J.B. Russ, H. Waisman, A novel topology optimization formulation for enhancing fracture resistance with a single quasi-brittle material, Internat. J. Numer. Methods Engrg. 121 (13) (2020) 2827–2856.
- [15] M.A. Bessa, R. Bostanabad, Z. Liu, A. Hu, D.W. Apley, C. Brinson, W. Chen, W.K. Liu, A framework for data-driven analysis of materials under uncertainty: Countering the curse of dimensionality, Comput. Methods Appl. Mech. Engrg. 320 (2017) 633–667.
- [16] A. Iyer, Y. Zhang, A. Prasad, P. Gupta, S. Tao, Y. Wang, P. Prabhune, L.S. Schadler, L.C. Brinson, W. Chen, Data centric nanocomposites design via mixed-variable Bayesian optimization, Mol. Syst. Des. Eng. 5 (8) (2020) 1376–1390.

- [17] L. Wang, S. Tao, P. Zhu, W. Chen, Data-driven topology optimization with multiclass microstructures using latent variable Gaussian process, J. Mech. Des. 143 (3) (2021) 031708.
- [18] G.A. Francfort, J.-J. Marigo, Revisiting brittle fracture as an energy minimization problem, J. Mech. Phys. Solids 46 (8) (1998) 1319–1342.
- [19] B. Bourdin, G.A. Francfort, J.-J. Marigo, Numerical experiments in revisited brittle fracture, J. Mech. Phys. Solids 48 (4) (2000) 797–826.
- [20] B. Bourdin, G.A. Francfort, J.-J. Marigo, The variational approach to fracture, J. Elasticity 91 (1–3) (2008) 5–148.
- [21] C. Miehe, M. Hofacker, F. Welschinger, A phase field model for rateindependent crack propagation: Robust algorithmic implementation based on operator splits, Comput. Methods Appl. Mech. Engrg. 199 (45–48) (2010) 2765–2778.
- [22] L. Wang, Y.-C. Chan, Z. Liu, P. Zhu, W. Chen, Data-driven metamaterial design with Laplace-Beltrami spectrum as "shape-DNA", Struct. Multidiscip. Optim. (2020) 1–16.

- [23] Y.-C. Chan, F. Ahmed, L. Wang, W. Chen, METASET: Exploring shape and property spaces for data-driven metamaterials design, J. Mech. Des. 143 (3) (2021) 031707.
- [24] B. Hassani, E. Hinton, A review of homogenization and topology optimization I—homogenization theory for media with periodic structure, Comput. Struct. 69 (6) (1998) 707–717.
- [25] N. Komodakis, N. Paragios, G. Tziritas, MRF energy minimization and beyond via dual decomposition, IEEE Trans. Pattern Anal. Mach. Intell. 33 (3) (2010) 531–552.
- [26] R.O. Ritchie, The conflicts between strength and toughness, Nature Mater. 10 (11) (2011) 817–822.
- [27] Z.P. Bazant, J. Planas, Fracture and size effect in concrete and other quasibrittle materials, 16, CRC Press, 1997.
- [28] H. Amor, J.-J. Marigo, C. Maurini, Regularized formulation of the variational brittle fracture with unilateral contact: Numerical experiments, J. Mech. Phys. Solids 57 (8) (2009) 1209–1229.